Journal of Geophysical Research: Solid Earth

Supporting Information for

Shear-Enhanced Electrical Conductivity of Synthetic Quartz-Graphite Gouges: Implications for Electromagnetic Observations in Carbonaceous Shear Zones

Jinyu Chen[1], Jianye Chen[1], Lu Yao[1], Xi Ma[1]

[1]State Key Laboratory of Earthquake Dynamics,

Institute of Geology, China Earthquake Administration, Beijing 100029, China.

Contents of this file

Introduction

The supporting information includes analytical data on the starting materials and experimental data details, as well as information on data processing, fitting, and data comparison.

Text S1. Experimental data processing

Due to slight assembly misalignment, the rotatory corundum cylinder often fluctuated at each frictional revolution. Thus, all frictional curves were smoothed using the moving-average method, which takes an average of data points with the window width corresponding to one revolution (Figure S2a, for more smoothing details see Yao et al., 2013). In addition, to investigate the frictional properties in the early stage, all mechanical data before the steady state were not smoothed. For LHV1372, three hold tests occurred in the slip displacements of 0.53, 1.97, and 2.97 m (black arrows in Figure S2a), with no noticeable changes in the mechanical and electrical behaviors.

Figure S2b shows the smoothed frictional coefficient data (μ, linear scale) and the raw electrical conductivity data (σ, log scale) plotted against slip displacement (D) for a 5 wt.% Gr-bearing specimen at 2.0 MPa (LHV1372). As the slip displacement increased to 0.57 m, μ rapidly increased to a peak value at first and then slightly decreased. Finally, a steady state was achieved, *i.e.*, μ remained stable within ±0.1 m until the eventual 3.21 m displacement (violet-shaded area). In contrast, σ grew logarithmically after the slip displacement of 0.23 m, increasing by eight orders of magnitude. Then, σ maintained until the end a conduction-steady-state within one order of magnitude variation from 0.79 m (red-shaded area).

To explain the mechanical–electrical properties of the specimens, we identified several critical parameters on all experimental curves. Taking the LHV1372 experiment as an example, (1) steady-state frictional coefficient (μ_{ss}) and steady-state electrical conductivity (σ_{ss}) were respectively obtained from the arithmetically average value of μ in steady-state and the logarithmically average value of σ in steady-state; (2) D when μ achieved μ_{ss} ($D_{\mu ss}$) and σ achieved σ_{ss} ($D_{\sigma ss}$). Occasionally, the determination of $D_{\mu ss}$, and thus μ_{ss}, suffered from the large fluctuations in the friction curves, in which case, we gained insight from the evolution of gouge layer thickness, which always showed exponential compaction in the displacement range of $D_{\mu ss}$ (pentagrams in Figure S3) and was expected to roughly share the characteristic displacement as that for friction (Marone, 1998); (3) interestingly, the σ curve showed large jumps from the initial level (σ_0) at short displacements, even before reaching the peak friction. Accordingly, we marked this displacement as $D_{\sigma ch}$, defined by more than two orders of magnitude σ-increase for $\sigma_0 < 0.01$ S/m and by a factor of 1.5 for $\sigma_0 > 0.01$ S/m.

Each set of μ (linear scale) and σ (log scale) curves of all experiments, as a function of slip displacement, are listed in Figures S4–S6. Due to technique bias for recorded data, all experimental data were managed with a translational correction; all initial friction coefficients were corrected to 0 and all frictional slips were corrected to start in 10^{-4} m. As the offsets were very small (<0.001 for μ and 10^{-8}–10^{-6} m for D), we believe this correction did not affect our experimental results. The corresponding critical parameters for each experiment (*i.e.*, μ_{ss}, $D_{\mu ss}$, σ_{ss}, $D_{\sigma ch}$, and $D_{\sigma ss}$) were located on the experimental curves of the aforementioned figures. Moreover, several specimens performed erratic frictional behaviors, *i.e.,* LHV2051, LHV2052, LHV2057, and LHV2429, due to (1) Qz particles leakage, (2) a part of the Teflon® components was cut in the slip surface, and (3) frictional resistance existed between PMMA (transparent vessel) and clamping. Therefore, these frictional curves (blue dashed lines in Figures S4–S6) were not shown in Figures 2–3 and were not applied to fit the equation in the discussion.

Text S2. Fitting details and experimental data comparison

Figures S7a and S7b show the μ_{ss} and the σ_{ss} plotted against X_{Gr} at 2 and 5 MPa for all specimens, respectively. A similar trend can be seen in the relationship between μ_{ss}/σ_{ss} and X_{Gr}

in the range of 2–5 MPa normal stress. Therefore, we concentrated all experimental data of 2 and 5 MPa for data fitting to explore the X_{Gr} dependency of μ_{ss} and σ_{ss}, respectively. Although μ_{ss} at 5 MPa was slightly higher than that at 2 MPa, we believe it does not affect our conclusions. In addition, we allowed the parameters μ_{ss}, σ_{ss}, and X_{Gr} for each specimen to vary within an optimization range during the fitting process. These ranges include the variabilities in the standard deviation of all experimental data and the uncertainties in adapting the X_{Gr} (within ±0.4%). Because a small quantity of Qz particles was inevitably extruded into the gaps between the outer electrode loop and rotary cylinder during the frictional slip, the mechanical data became oscillatory during the frictional slip, especially for the specimens with low to intermediate Gr contents (< 10 wt.%) (Figures 2–3). As a result, the μ_{ss} values of the low-X_{Gr} mixtures were higher and more scattered than those of Oohashi et al. (2013) (0.53–0.85, orange regime in Figure S7a). Therefore, μ_{Qz} (0.73) was taken to be the mean value of μ_{ss} for the low-X_{Gr} specimens (< 13.6 vol.%).

All fitted parameters of Equation 2 and Equation 3 in this study are shown in Table 3 and Table 4, respectively. The friction of pure Gr flakes was consistent with that in Oohashi et al. (2013)'s results (0.08–0.16). Our X_{cw}-value (22.3 vol.%) and S-value (8.97) were higher than Oohashi et al. (2013)'s values (X_{cw} = 11.8–12.8 vol.%, S = 1.56–1.82, for a range of slip rate 0.2–56 mm/s), indicating higher critical value but more rapid weakening. Meanwhile, our critical Gr volume fraction for a dramatic decrease of the frictional coefficient (~13.6 vol.%) (grey dashed lines in Figure S7a) was higher than that observed by Oohashi et al. (2013) (~5 vol.%). It might be related to the difference in the grain size of Qz particles used in the experiment, i.e., the Qz grain size of their experimental specimens (<200 μm) was approximately an order of magnitude greater than ours (12.2 μm). Gouges with larger Qz particles tend to have a smaller specific surface area, which requires a smaller amount of Gr to attain an *ad-hoc* microstructure that leads to lubrication of the gouge. This is also supported by a recent study (Chen, 2022). It implies that the grain size of strong Qz particles is also a pivotal character in determining the frictional stability of Gr-bearing gouges.

The σ values of pure Qz particles (1.1×10^{-10} S/m–2.7×10^{-10} S/m) and of pure Gr flakes (~10^3 S/m) were stable and were close to previous static compaction experimental data under 0.1–300 MPa (Chen et al., 2017). The fitting of the σ_{ss}-X_{Gr} curve yielded an r-value of 3.36, which is slightly higher than that obtained from static compaction of Qz-Gr mixtures, 2.53 (Chen et al., 2017), and lower than that of Gr-bearing olivine aggregates under high pressure and temperature conditions, ~10 (Wang et al., 2013). Interestingly, the α-value was 1.29, much lower than that of the above-mentioned studies (3.39 and 10–20). We propose the following explanation for such difference: From the percolation theory, the conductivity of a mixture increases substantially once thin disk-shaped Gr grains are interconnected at edges (Gueguen & Dienes, 1989). The α-values can be converted to the ratio of the average diameter (c) to the thickness (w) for the Gr disks ($c/w = \alpha/(\pi/4)$) (Wang et al., 2013). In this study, our c/w value (1.67) is inconsistent with the geometry of the traditional conductive structure of interconnected grain-boundary carbon films (c/w>10) (Duba & Shankland, 1982; Frost et al., 1989; Mareschal et al., 1992). Because the direction of the conductive pathway in the SLZ in this experiment was parallel to the direction of the Gr disks, the c/w defined by the α from Equation 3 was not the average diameter-thickness ratio of the Gr disks, but rather the major axis-minor axis ratio of the Gr disks. Therefore, the c/w ratio reflects the geometry of the actual conductive channel.

The percolation threshold value (X_c) was determined based on our experimental results: The σ_{ss} of the specimen with 4 wt.% Gr was very high (10^{-3} S/m), while the σ_{ss} of the specimen with 3 wt.% Gr maintained a low value (~10^{-11} S/m) throughout most of the slip displacement range and only slightly increased at the end (> 10^{-8} S/m) (Figure 2d), suggesting that some of the Gr flakes can locally develop connected fabric. Therefore, we roughly determined the Gr weight fraction of 3 wt.% (corresponding to a volume fraction of 3.4 vol.%) as the percolation threshold value (X_c) of the relationship between σ_{ss} and X_{Gr}. In this study, the X_c is a fixed value. However, compared with the X_c under static compaction (Figure 3b), normal stress and shear strain significantly influence it. We interpreted the abrupt enhancement of the electrical conductivity as due to the fabric of "GCCs", i.e., the Gr-interconnectivity has something to do with the geometry (i.e., aspect ratio) of the Gr flakes over the surface area of individual Qz particles in the shear zone. Normal stress or static compaction can reduce the porosity of Qz particles and increase the interconnectivity of Gr flakes. In contrast, shear deformation can enhance the aspect ratio of Gr flakes, which leads to higher interconnectivity of grain-boundary Gr flakes and lower percolation threshold of the mixture compared with static compaction (decrease from 6.0 to 3.4 vol.% in Figure 8).

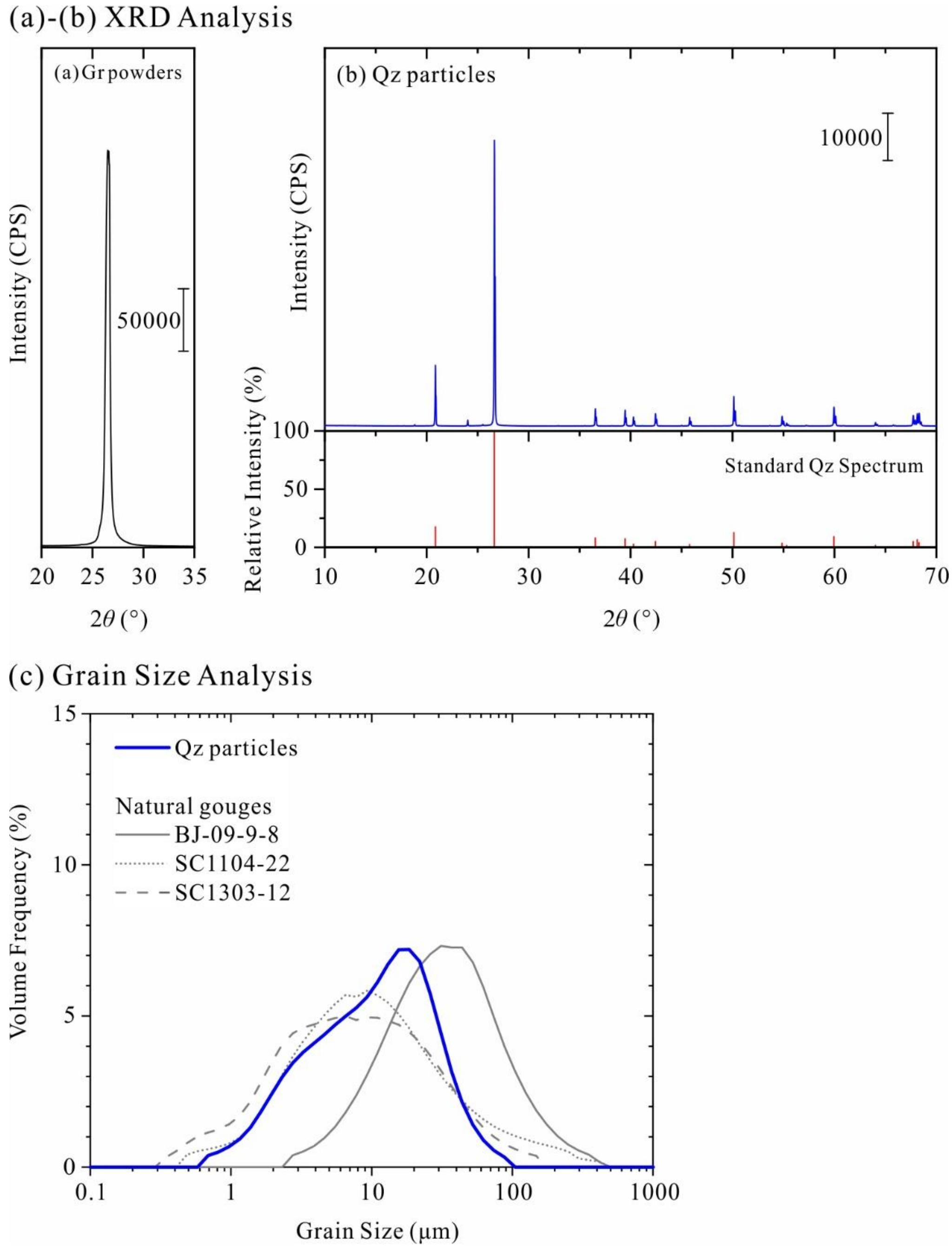

Figure S1. Analytical data of the starting materials used for the experiments. (a) X-ray diffraction spectrum of Gr and (b) Qz particles compared with the standard Qz spectrum. (c) Particle size distribution of the Qz particles (blue line). Grey lines represent natural gouges collected from the coseismic slip zone of the Yingxiu–Beichuan fault zone in Sichuan province, China P.R. (Chen et al., 2017).

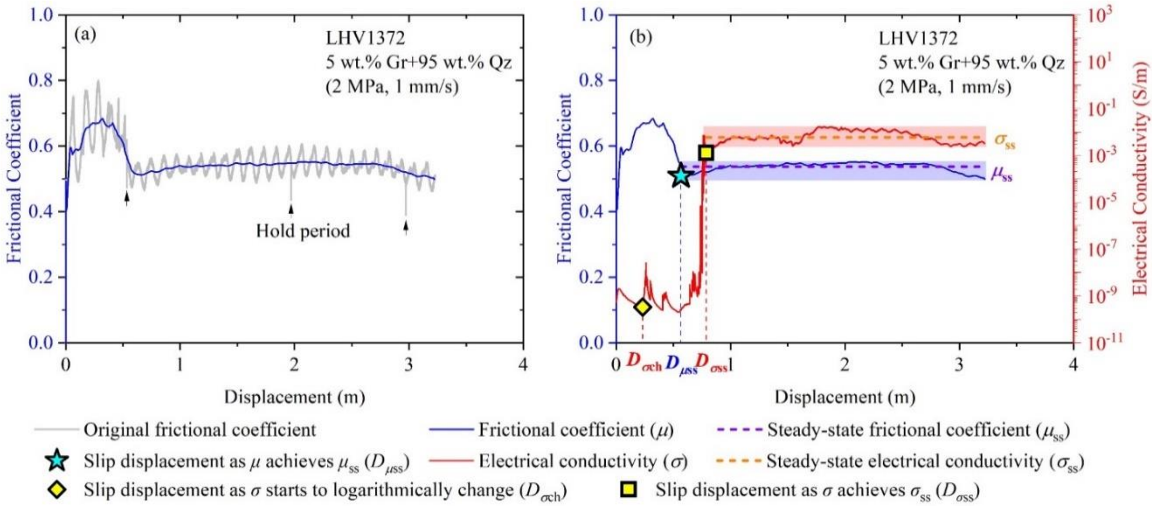

Figure S2. Experimental data curves of 5 wt.% Gr-bearing specimen (LHV1372) at 2 MPa and 1 mm/s as a function of slip displacement. This figure illustrates mechanical data smoothing and the obtained critical parameters. (a) Original (light grey line) *vs* smoothed (blue line) friction data. The experimental data in the hold period (v_e < 0.6 mm/s) are pointed by black arrows, and they were removed in smoothed processing. (b) Evolution of smoothed frictional coefficient (μ, blue line) on a linear scale and electrical conductivity (σ, red line) on a log scale. The dashed violet line, dashed orange line, blue pentagram symbol, yellow diamond symbol, and yellow square symbol located on the curve indicate μ_{ss}, σ_{ss}, $D_{\mu ss}$, $D_{\sigma ch}$, and $D_{\sigma ss}$, respectively.

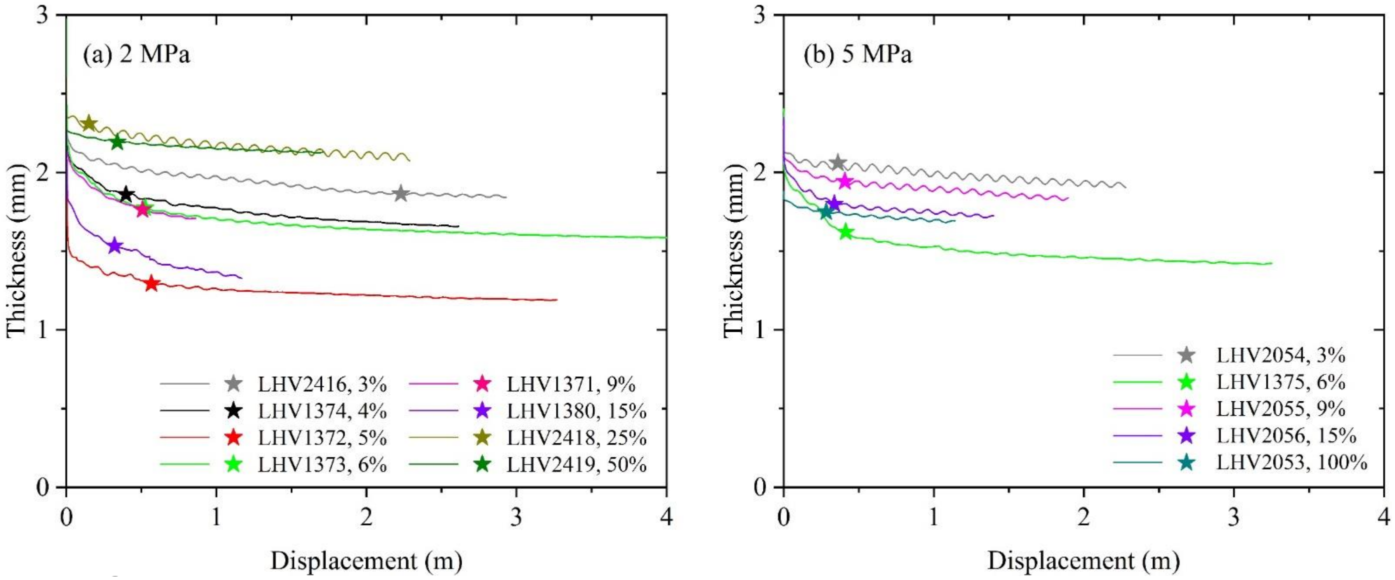

Figure S3. Evolution of thickness as a function of slip displacement during a progressive fault slip. This figure shows results for all experiments performed at a normal stress of (a) 2 MPa and (b) 5 MPa. The pentagram symbols identify the critical points of thickness evolution, *i.e.*, transformed from the exponential decreases to the linear reductions, which are expected to have similar characteristic displacement as that for friction. The numerical percentages of the legends indicate the Gr weight percentages of experimental specimens.

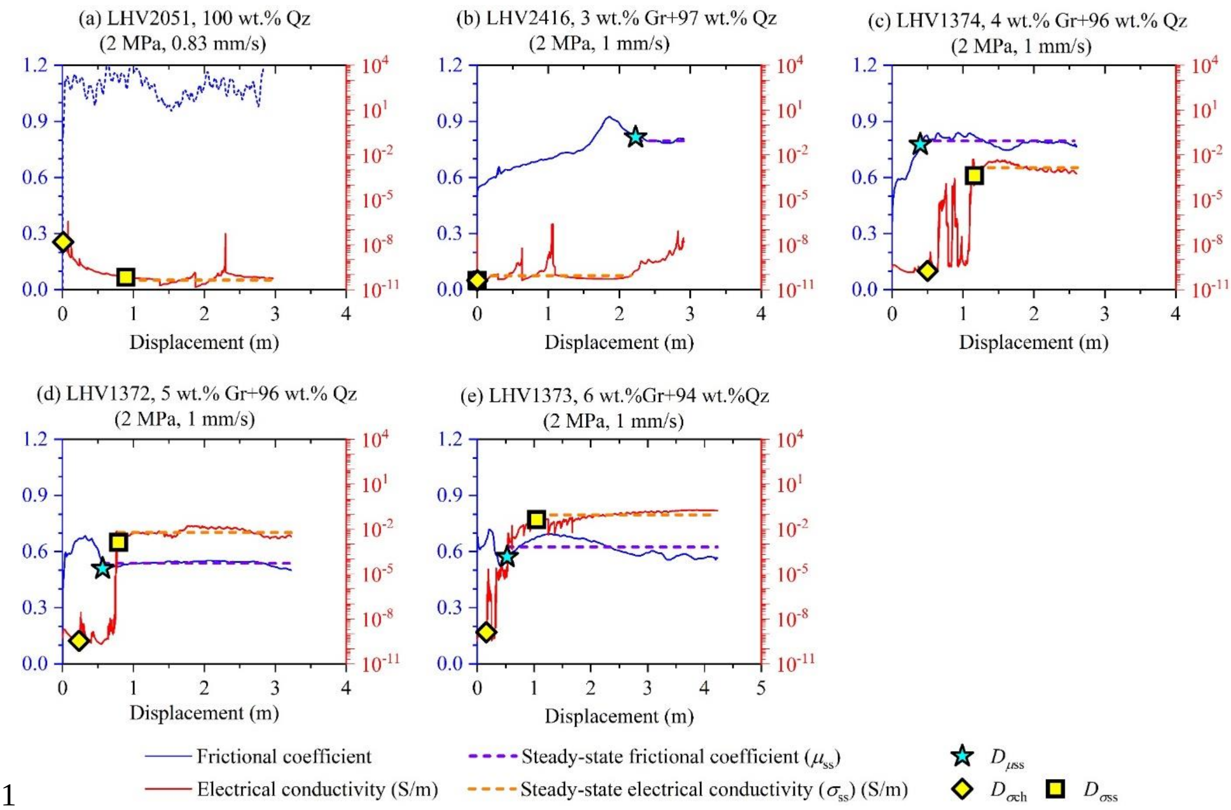

Figure S4. Frictional coefficient-electrical conductivity *vs* slip displacement for dry Gr–Qz mixtures at 2 MPa and 0.83–1.00 mm/s. The Gr fractions of mixtures include (a) 0 wt.%, (b) 3 wt.%, (c) 4 wt.%, (d) 5 wt.%, and (e) 6 wt.%. The erratic frictional behavior of LHV2051 in (a) is shown in a blue dashed line. Legends are identical to those in Figure S2.

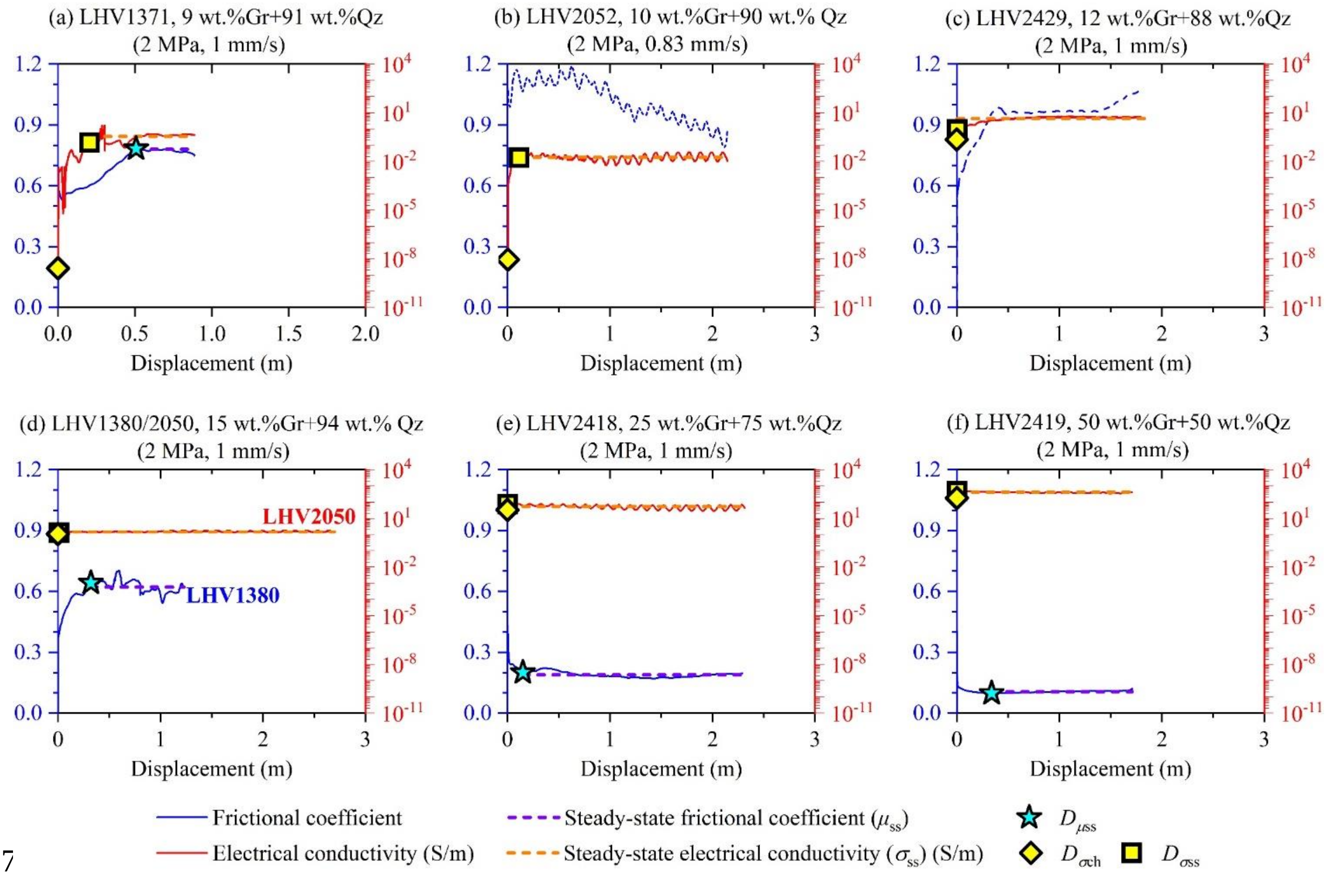

Figure S5. Frictional coefficient-electrical conductivity plotted against slip displacement for dry Gr–Qz mixtures at 2 MPa and 0.83–1.00 mm/s. The Gr fractions of mixtures include (a) 9 wt.%, (b) 10 wt.%, (c) 12 wt.%, (d) 15 wt.%, (e) 25 wt.% and (f) 50 wt.%. The erratic frictional behavior of LHV2052 and LHV2429 in panels b and c are shown in a blue dashed line. The friction-conductivity data of the 15 wt.% Gr-bearing specimens were obtained from two experiments, *i.e.*, LHV1380 and LHV 2050. Legends are identical to those in Figure S2.

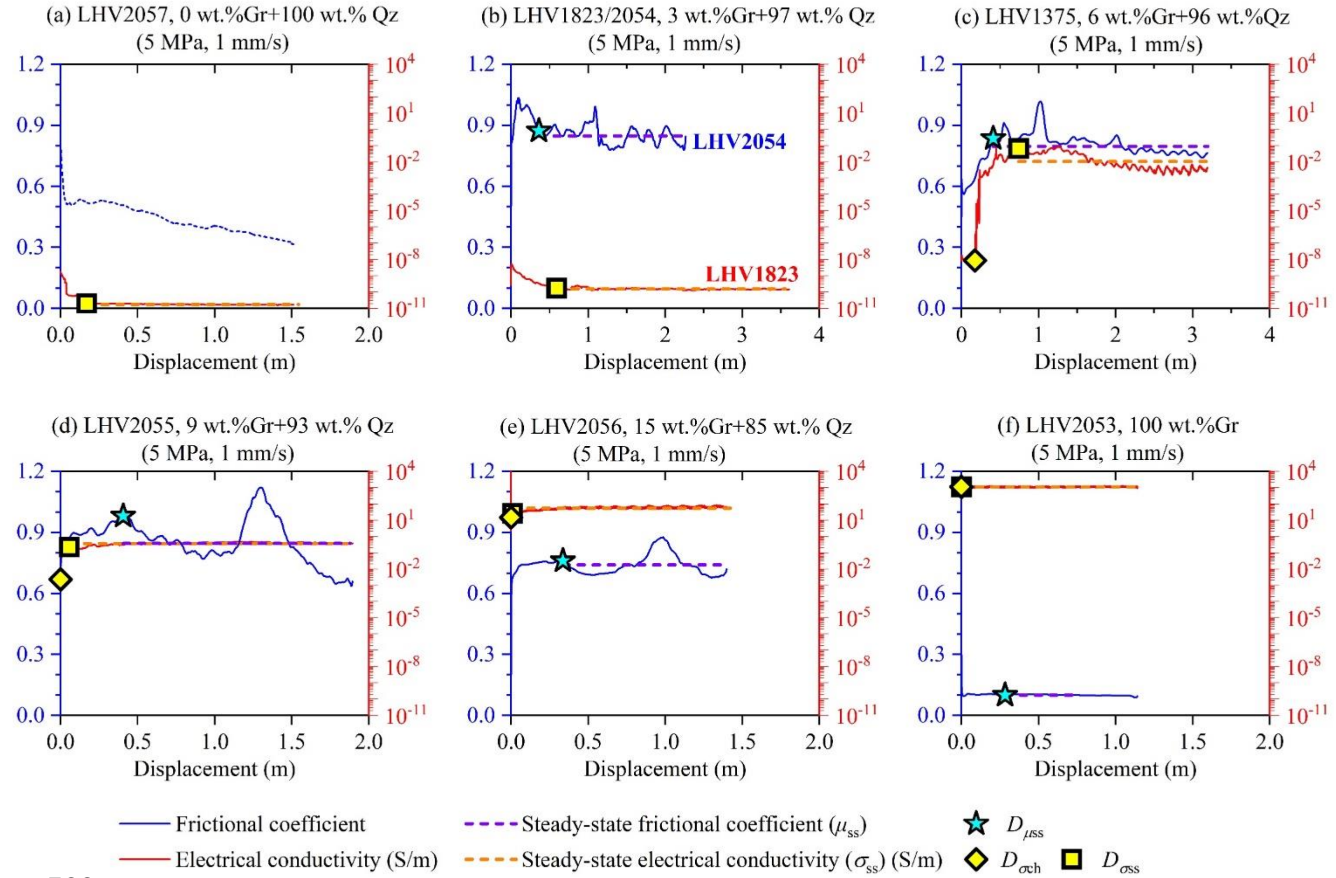

Figure S6. Frictional coefficient–electrical conductivity plotted against slip displacement for dry Gr–Qz mixtures at 5 MPa and 1 mm/s. The Gr fractions of mixtures include (a) 0 wt.%, (b) 3 wt.%, (c) 6 wt.%, (d) 9 wt.%, (e) 15 wt.% and (f) 100 wt.%. The erratic frictional behavior of LHV2057 in (a) is shown in a blue dashed line. The friction–conductivity data of the 3 wt.% Gr-bearing specimen was obtained from two experiments, *i.e.*, LHV1823 and LHV 2054. Legends are identical to those in Figure S2.

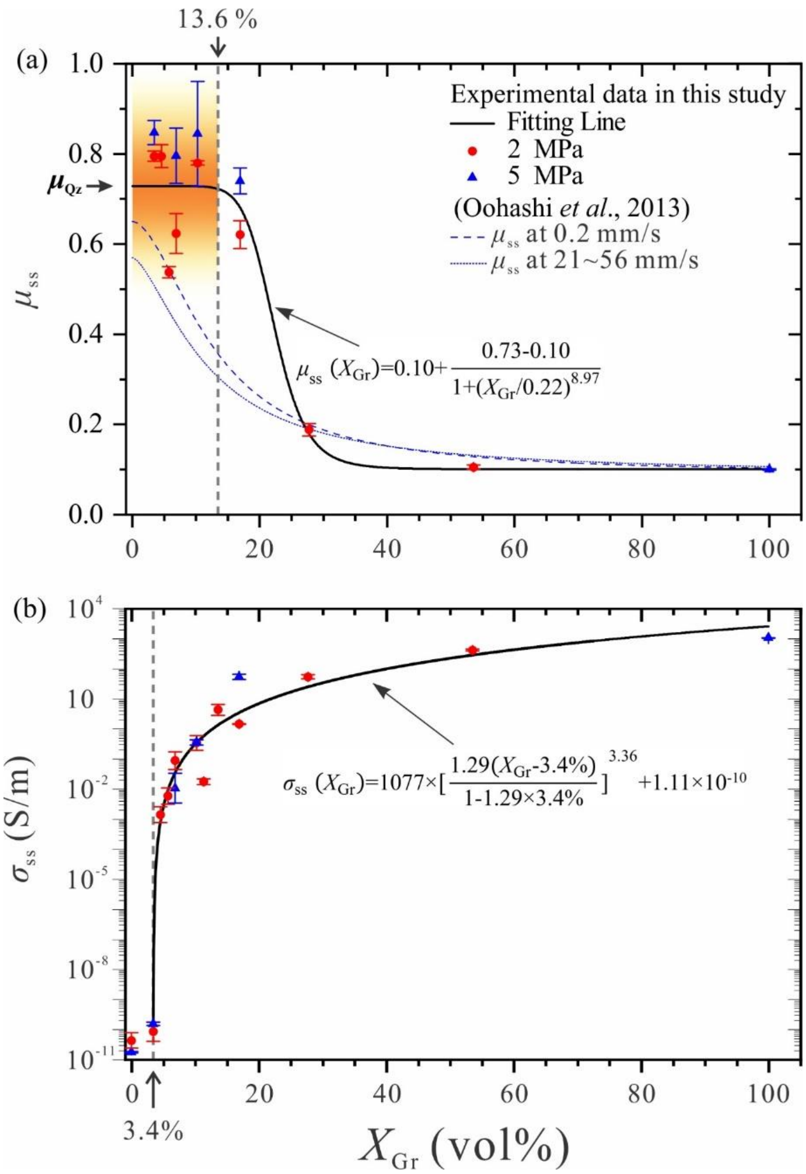

Figure S7. Effect of X_{Gr} on (a) μ_{ss} and (b) σ_{ss} of the Gr–Qz mixtures at 2 (red circular symbols) and 5 MPa (blue triangular symbols). Error bars indicate the variabilities in the standard deviation of all experimental data. Black solid curves in panels a and b display the fit to each data set with Equation 1 and Equation 2, respectively. The μ_{ss}–X_{Gr} relationship of Qz-Gr mixtures at 0.2 and 21–56 mm/s under similar environmental conditions proposed by Oohashi et al. (2013) were drawn by blue dashed and dotted lines, respectively. An orange area identifies the potential distributed range of μ_{Qz}.

References

Chen, J.-Y., Yang, X.-S., & Chen, J.-Y. (2017). Experimental studies on the relationship between carbonaceous structure and electrical conductivity of the Longmenshan fault zone, *Chinese J. Geophys. (in Chinese)*, *60*(9), 3475-3492. https://doi.org/10.6038/cjg20170917.

Chen, J. (2022). The Effect of Quartz Particle Size on the Frictional and Electrically Conductive Properties of Mixed Graphite–Quartz Gouges, *Front. Earth Sci.*, *10*, 913315. https://doi.org/10.3389/feart.2022.913315.

Duba, A. G., & Shankland, T. J. (1982). Free carbon & electrical conductivity in the Earth's mantle, *Geophys. Res. Lett.*, *9*(11), 1271-1274. https://doi.org/10.1029/GL009i011p01271.

Frost, B. R., Fyfe, W. S., Tazaki, K., & Chan, T. (1989). Grain-boundary graphite in rocks and implications for high electrical conductivity in the lower crust, *Nature*, *340*(6229), 134-136. https://doi.org/10.1038/340134a0.

Gueguen, Y., & Dienes, J. (1989). Transport properties of rocks from statistics and percolation, *Math Geol*, *21*(1), 1-13. https://doi.org/10.1007/BF00897237.

Mareschal, M., Fyfe, W. S., Percival, J., & Chan, T. (1992). Grain-boundary graphite in Kapuskasing gneisses and implications for lower-crustal conductivity, *Nature*, *357*, 674-676. https://doi.org/10.1038/357674a0.

Marone, C. (1998). Laboratory-derived friction laws and their application to seismic faulting, *Annu. Rev. Earth Planet Sci.*, *26*(1), 643-696. https://doi.org/10.1146/annurev.earth.26.1.643.

Oohashi, K., Hirose, T., & Shimamoto, T. (2013). Graphite as a lubricating agent in fault zones: An insight from low- to high-velocity friction experiments on a mixed graphite-quartz gouge, *J. Geophys. Res. Solid Earth*, *118*, 1-18. https://doi.org/10.1002/jgrb.50175.

Wang, D., Karato, S.-i., & Jiang, Z. (2013). An experimental study of the influence of graphite on the electrical conductivity of olivine aggregates, *Geophys. Res. Lett.*, *40*(10), 2028-2032. https://doi.org/10.1002/grl.50471.

Yao, L., Ma, S., Shimamoto, T., & Togo, T. (2013). Structures and high-velocity frictional properties of the Pingxi fault zone in the Longmenshan fault system, Sichuan, China, activated during the 2008 Wenchuan earthquake, *Tectonophysics*, *599*, 135-156. https://doi.org/10.1016/j.tecto.2013.04.011.